

Multifunctional $[(\text{CH}_3)_3\text{S}][\text{FeCl}_4]$ Plastic Crystal for Solar Thermal and Electric Energy Storage

Jorge Salgado-Beceiro, **Juan Manuel Bermudez Garcia**, **Antonio Llamas-Saiz**, Socorro Castro-Garcia, Maria Antonia Señaris-Rodriguez, Francisco Rivadulla, Manuel Sanchez-Andujar

Submitted date: 19/08/2020 • Posted date: 20/08/2020

Licence: CC BY-NC-ND 4.0

Citation information: Salgado-Beceiro, Jorge; Bermudez Garcia, Juan Manuel; Llamas-Saiz, Antonio; Castro-Garcia, Socorro; Señaris-Rodriguez, Maria Antonia; Rivadulla, Francisco; et al. (2020): Multifunctional $[(\text{CH}_3)_3\text{S}][\text{FeCl}_4]$ Plastic Crystal for Solar Thermal and Electric Energy Storage. ChemRxiv. Preprint.
<https://doi.org/10.26434/chemrxiv.12830288.v1>

In this work, we report a new halometallate $[(\text{CH}_3)_3\text{S}][\text{FeCl}_4]$ with plastic crystal behaviour as a new material for multi-energy storage. This material undergoes a first-order solid-solid plastic crystal phase transition near room temperature with a relatively large latent heat ($\sim 40 \text{ kJ kg}^{-1}$) and an operational temperature for storing and releasing thermal energy between 42°C (315 K) and 29°C (302 K), very appropriate for solar thermal energy storage. In addition, the dielectric, magnetization and electron spin resonance studies reveal that this material exhibits multifunctional properties with temperature-induced reversible changes in its dielectric, conducting and magnetic behaviour associated with the phase transition. Also, the dielectric permittivity increases sharply up to 5 times when inducing the phase transition, which can be exploited to store electric energy into a capacitor. Therefore, $[(\text{CH}_3)_3\text{S}][\text{FeCl}_4]$ is a very interesting compound with coexistence of multifunctional properties that can be useful for both solar thermal and electric energy storage.

File list (1)

Preprint_Multifunctional TES.pdf (2.00 MiB)

[view on ChemRxiv](#) • [download file](#)

Multifunctional $[(\text{CH}_3)_3\text{S}][\text{FeCl}_4]$ plastic crystal for solar thermal and electric energy storage

Jorge Salgado-Beceiro^{1,‡}, Juan Manuel Bermúdez-García^{1,‡*}, Antonio Luis Llamas-Saiz², Socorro Castro-García¹, María Antonia Señarís-Rodríguez¹, Francisco Rivadulla³, Manuel Sánchez-Andújar^{1**}

1. University of A Coruña, QuiMolMat Group, Dpt. Chemistry, Faculty of Science and Advanced Scientific Research Center (CICA), Zapateira, 15071 A Coruña, Spain.

2. RIAIDT X-ray Unit, Universidade de Santiago de Compostela, 15782 Santiago de Compostela, Spain.

3. Centro Singular de Investigación en Química Biolóxica e Materiais Moleculares (CiQUS), Departamento de Química-Física, Universidade de Santiago de Compostela. 15782 Santiago de Compostela (Spain)

‡ These authors have equally contributed to this work.

*j.bermudez@udc.es, **m.andujar@udc.es

Supporting Information (SI) available: PXRD patterns obtained at room temperature, thermogravimetric curves, additional crystallographic figures and tables.

In this work, we report a new halometallate $[(\text{CH}_3)_3\text{S}][\text{FeCl}_4]$ with plastic crystal behaviour as a new material for multi-energy storage. This material undergoes a first-order solid-solid plastic crystal phase transition near room temperature with a relatively large latent heat ($\sim 40 \text{ kJ kg}^{-1}$) and an operational temperature for storing and releasing thermal energy between 42°C (315 K) and 29°C (302 K), very appropriate for solar thermal energy storage. In addition, the dielectric, magnetization and electron spin resonance studies reveal that this material exhibits multifunctional properties with temperature-induced reversible changes in its dielectric, conducting and magnetic behaviour associated with the phase transition. Also, the dielectric permittivity increases sharply up to 5 times when inducing the phase transition, which can be exploited to store electric energy into a capacitor. Therefore, $[(\text{CH}_3)_3\text{S}][\text{FeCl}_4]$ is a very interesting compound with coexistence of multifunctional properties that can be useful for both solar thermal and electric energy storage.

1. Introduction

Hybrid halometallate systems, which are composed of coordination metal halide anions and organic cations, have attracted great interest due to their potential applications in a wide variety of fields. For example, the low melting temperature of some hybrid halometallate salts has been exploited in the field of the ionic liquids.^{1–4}

Additionally, the existence of different functional properties (such as dielectric, magnetic, optical or caloric properties), associated to the reversible solid-solid phase transitions they often possess, renders them very interesting phase change materials (PCMs) for sensors and transducers, memory devices, photonics and optoelectronics, and thermal energy storage (TES), among others applications.^{5–10} In this regard, hybrid halometallates resemble the emerging family of hybrid organic-inorganic perovskites, whose functionality is also related to structural solid-solid phase transitions, in many cases of order-disorder type.^{11–13} However, differently from the framework structure presented by the perovskite compounds, the molecular nature of the hybrid halometallates, with weakly associated inorganic anions and organic cations, allows for a much larger orientational or conformational degree of freedom, which finally results in the possibility of appearance of soft “plastic” crystals.¹⁴

This is a mesophase between the crystalline and the liquid state often found in ionic compounds with large molecular moieties, which acquire some rotational degree of freedom above a certain temperature, while their center of gravity remains fixed in the crystal lattice.¹⁵

Very interestingly, different hybrid halometallate with plastic crystal behaviour have been recently reported to display outstanding dielectric properties at room temperature, such as ferroelectricity and piezoelectricity.^{16–19} Moreover, these compounds can be obtained by easy and low cost methods as thin-films, which is desirable for practical applications.²⁰

Additionally, the relative high latent heat associated to such solid-solid phase transitions in hybrid halometallates can be useful for TES applications.^{21,22} Up to date, most materials used for TES applications are those with solid-liquid phase transitions, mainly because the latent heat is larger than in the case of solid-solid transitions. Nevertheless, there is an increasing interest in developing TES materials with solid-solid phase transitions because they offer a number of advantages: they avoid leaks and/or volatilization of the liquid phase, minimise volume changes providing denser and more compact systems, avoid incongruent melting, and increase thermal stability.^{23–25} Despite all these advantages, it remains a challenge to find new solid-solid PCMs with sufficient latent heat^{26–28} and an adequate operational temperature.^{29,30}

In this context, hybrid halometallates are arising as promising materials that can combine TES and multifunctional properties, and which are of great interest for technological applications,³¹ even if these materials are very scarce.⁵

In this work, we report the synthesis and characterization of a new halometallate $[(\text{CH}_3)_3\text{S}][\text{FeCl}_4]$ with plastic crystal behaviour and interesting functional properties. As we demonstrate in this paper, this material shows a solid-solid plastic crystal phase transition with a relatively large latent heat ($\sim 40 \text{ kJ kg}^{-1}$) and an operational temperature that ranges between 42 and 29 °C (315 and 302 K). As we discuss below such temperature window matches very well with the requirements for commercial solar TES applications. In addition, the multifunctional properties exhibited by this compound (with a temperature-induced reversible change in its dielectric, conducting and magnetic behaviour), render this materials very interesting not only for thermal energy storage but also for electric energy storage.

2. Experimental section

2.1. Experimental section

Commercially available analytical grade $[(\text{CH}_3)_3\text{S}]\text{Br}$ (98% Sigma-Aldrich), $\text{FeCl}_3 \cdot 6\text{H}_2\text{O}$ (98% Sigma-Aldrich) and HCl solution (ca. 37 % in H_2O ACS reagent, ACROS Organics) were used as starting materials.

2.2 Synthesis of $[(\text{CH}_3)_3\text{S}][\text{FeCl}_4]$

Single crystals and polycrystalline powder of $[(\text{CH}_3)_3\text{S}][\text{FeCl}_4]$ have been obtained by crystallization from a water solution. For this purpose, stoichiometric amounts of $[(\text{CH}_3)_3\text{S}]\text{Br}$ and $\text{FeCl}_3 \cdot 6\text{H}_2\text{O}$ were dissolved by adding 3 ml of water and 3ml of hydrochloric acid. Rhombohedral yellow single crystals of $[(\text{CH}_3)_3\text{S}][\text{FeCl}_4]$ were obtained upon slow evaporation of the solvent at room temperature after several days and they were collected by filtration and washed several times with diethyl ether.

2.4. Thermal analysis

Thermogravimetric analyses (TGA) were carried out in a TGA-DTA Thermal Analysis SDT2960 equipment. For each experiment, approximately 27 mg of grounded single crystals were heated at a rate of 5 K min^{-1} from 300 K to 1200 K, using a corundum crucible, under a flow of dry nitrogen. Differential scanning calorimetric (DSC) analyses were carried out in a TA-Instruments Q200, heated and cooled with a rate of 1.5 K min^{-1} , from 270 up to 350 K, under a nitrogen atmosphere.

2.5. Powder X-ray diffraction

Powder X-ray diffraction (PXRD) patterns of the obtained polycrystalline samples were collected in a Siemens D-5000 diffractometer using $\text{CuK}\alpha$ radiation at room temperature. Comparison of experimental PXRD pattern with single crystal XRD pattern simulated using Mercury software³² confirmed the purity of the studied single phase samples (see Figure S1 of SI).

2.6. Single crystal X-ray diffraction

Single-crystal X-ray diffraction (SCXRD) experiments were carried out at temperatures well below and above the observed DSC transitions. For that purpose, single-crystal diffraction data sets of one crystal were collected at 100 K, 150 K, 200 K, 250 K, 300 K, 310 K and 320 K in a Bruker D8 VENTURE Kappa X-ray diffractometer equipped with a PHOTON III detector and using monochromatic $\text{MoK}\alpha$ radiation ($\lambda=0.71073 \text{ \AA}$).

A suitable crystal was chosen and mounted on a MiTeGen MicroMountTM using Paratone[®] N (Hampton Research). The temperature of the crystal was changed at 200 K h^{-1} rate blowing the sample with a stream of nitrogen gas from an Oxford Cryosystem 800 Plus cooler. The data integration and reduction were performed using the APEX3 v2019.1-0 (Bruker AXS, 2019) software suite. The integrations of the reflections were performed with SAINT 8.40A and the intensities collected were corrected for Lorentz and polarization effects and for absorption by semi-empirical methods on the basis of symmetry-equivalent data using SADABS 2016/2 of the suite software. The structures were solved by the dual-space algorithm implemented in SHELXT2014/5³³ program and were refined by least squares method on SHELXL2018/3.³⁴

To refine the structures, anisotropic thermal factors were employed for the non-H atoms. The hydrogen atoms of the $(\text{CH}_3)_3\text{S}^+$ cations were found in the Fourier difference maps except those belonging to the lowest occupancy positions in disordered cations. The coordinates of all H atoms were freely refined in the structure at 100 K and some of them were restrained at higher temperatures during the refinement using the riding model implemented in SHELXL2018/3. Their

isotropic displacement parameters were kept constrained to 1.5 times the U_{eq} values of the carbon atoms they are bonded.

Detailed experimental crystallographic data for $[(CH_3)_3S][FeCl_4]$ at $T = 100, 150, 200, 250, 300, 310$ and 320 K is included in Tables S1 of SI. CCDC 2000618-2000623 contains the supplementary crystallographic data for this paper. These data can be obtained free of charge from The Cambridge Crystallographic Data Centre via www.ccdc.cam.ac.uk/structures

2.6 Electron Spin Resonance

Electron Spin Resonance (ESR) experiments were performed between 130 K and 400 K in a Bruker EMX spectrometer operating at 9.4 GHz (X-band), equipped with an ER 4102ST resonant cavity (TE₁₀₂ mode). The linewidth, ΔH , was measured as the peak-to-peak distance in the first derivative of the absorption line, ΔH_{pp} .

2.9 Magnetic measurements

Variable-temperature magnetic susceptibility measurements were performed using a Quantum Design MPMS SQUID magnetometer. Different zero field-cooling /field-cooling as well as field-cooling/warming runs were performed between 4.2 K and 400 K, under different magnetic fields of $H = 0.1$ to 1 T.

2.7. Dielectric properties

The complex dielectric permittivity ($\epsilon_r = \epsilon'_r - i \epsilon''_r$) of cold-press pelletized samples was measured as a function of frequency and temperature with a parallel-plate capacitor coupled to a Solartron1260A Impedance/Gain-Phase Analyzer, capable to measure in the frequency range from 1 Hz up to 1 MHz using an amplitude of 1 V. The capacitor was mounted in a Janis SVT200T cryostat refrigerated with liquid nitrogen and with a Lakeshore 332 incorporated to control the temperature from 100 K up to 400 K. The data were collected on heating and before carrying out the measurement, the pellets were maintained at each temperature for two minutes, so as to allow them to reach thermal equilibrium. Pelletized samples, with an area of approximately 133 mm² and a thickness of approximately 1 mm, were prepared by cold-press to fit into the capacitor. Gold was sputtered previously on the surfaces of the pelletized samples to ensure a good electrical contact. All the dielectric measurements were carried out in a nitrogen atmosphere, performing several cycles of vacuum and nitrogen gas to ensure a sample environment free of water. The conductance of the sample was determined from the real axis intercept in the Nyquist plot of the impedance data.

3. Results and discussion

3.1. Thermal characterization

DSC experiments reveal that $[(CH_3)_3S][FeCl_4]$ undergoes a reversible first-order phase transition near room temperature, as shown by an endothermic peak on heating ($T_h = 315$ K) and an exothermic peak on cooling ($T_c = 302$ K) with a thermal hysteresis of 13 K (see Figure 1). This transition is fully reversible as indicated by the DSC cyclability and PXRD patterns (see Figure S2 of SI).

The values of the associated latent heat (ΔH) and entropy change (ΔS), obtained from the peak integration of the heat flow curves, are $\Delta H_h = 39.7$ kJ kg⁻¹ and $\Delta H_c = 40.7$ kJ kg⁻¹, $\Delta S_h = 126.0$ J kg⁻¹ K⁻¹ and $\Delta S_c = 134.3$ J kg⁻¹ K⁻¹.

Considering the configurational entropy as the main contributor to ΔS across the transition, the ratio of configurations or free energy minima thermally accessible to the system above/below the transition temperature, N , can be estimated from the equation $\Delta S = R \ln(N)$. We obtained a value of $N = 64$, which indicates a very large variation in the number of available states in the high temperature phase, characteristic of plastic crystals.⁵

Additionally, the characteristic plastic deformation of plastic crystal state can be observed by bending a pelletized sample previously heated above T_t , see video S1 of SI.

In this context, according to the TGA results (Figure S3 of SI), the new $[(CH_3)_3S][FeCl_4]$ compound shows a large thermal stability with a decomposition temperature of $T_{dec} \sim 550$ K, offering a thermal stability of between 50 and 20 K larger than most of the reported hybrid halometallates, see Table 1.

Above this temperature, it decomposes in two steps: there is a first weight loss ($\sim 70\%$ at $T \sim 550$ K), which corresponds to the loss of the $[(\text{CH}_3)_3\text{S}]^+$ cations and one Cl^- anion; and a second weight loss ($\sim 30\%$ at $T \sim 773$ K) related to the complete volatilization of the remaining inorganic FeCl_3 residue. Along the same line, the DTA results (Figure S3 of SI), show endothermic processes upon heating related to the thermally-induced phase transition and the thermal decomposition of the material.

In view of such phase transition and in order to evaluate the potential of this compound for TES applications, we start by analysing the requirements and the commercial needs for solar TES materials.

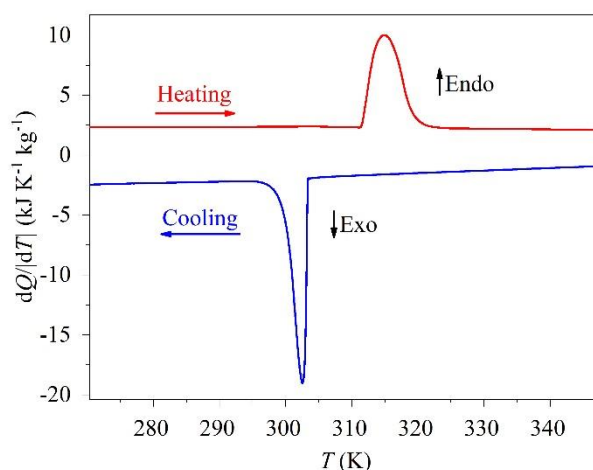


Figure 1. DSC results as a function of temperature, obtained by heating and cooling the sample at a rate of 1.5 K min^{-1} .

In this context, the ideal thermal storage material should fulfill several criteria related to its thermal and physico-chemical properties, namely: phase transition temperature in the desired operating range and thermal hysteresis ($T_h - T_c$) matching the desired charging and discharging temperatures, large specific heat and phase transition latent heat, large density to increase the thermal storage per unit of volume, large thermal conductivity, small volume change at the phase transition, low vapour pressure and chemical and thermal stability, among others.^{23,39,40}

As for the commercial needs for TES, PCMs for household applications (such as indoor comfort temperature or hot water supply) are required to store thermal energy at operational temperatures (charging temperatures) of around $30\text{--}60^\circ\text{C}$ ($303\text{--}333$ K).³⁰ These temperatures are easily achievable under sunlight illumination without needing the use of solar collectors. Besides, the temperature for releasing the stored thermal energy (discharging temperature) should be around two degrees above the desired comfort temperature (normally around 20°C or 293 K).³⁰

The thermal and physico-chemical parameters of $[(\text{CH}_3)_3\text{S}][\text{FeCl}_4]$ that are of interest for TES applications are summarized in Table 1, where our material is compared with other outstanding hybrid halometallate compounds.

As it can be seen in Table 1 and Figure 2a, the latent heat per unit of mass of $[(\text{CH}_3)_3\text{S}][\text{FeCl}_4]$ is larger than most hybrid halometallate compounds, even if the specific heat capacity is expected to be similar, $1.0 - 1.5 \text{ kJ kg}^{-1} \text{ }^\circ\text{C}^{-1}$.⁵

Additionally, due to its relatively large density, the latent heat per unit of volume is also amongst the largest values in hybrid halometallates. Most interestingly, the operational temperature of this compound for storing thermal energy (charging temperature) is ~ 315 K, and for releasing this energy (discharging temperature) is ~ 302 K, which is very close to operational temperature requirements for solar TES applications, especially for domestic use³⁰, as indicated above (see Figure 2b). Therefore, the large latent heat and the enhanced thermal stability and operational temperature in comparison with most reported hybrid halometallates bring this material closer to the commercial requirements for solar thermal energy storage applications.

Table 1. Selected thermal and physico-chemical parameters of interest for TES applications for different hybrid halometallate compounds: transition temperature (T_h) and thermal hysteresis ($T_h - T_c$), phase transition latent heat per unit of mass and per unit of volume (ΔH_h), density of the low temperature polymorphs (ρ) and decomposition temperature (T_{dec}).

Hybrid halometallate compounds	T_h (K)	$T_h - T_c$ (K)	ΔH_h (kJ kg ⁻¹)	ΔH_h (J cm ⁻³)	ρ (g cm ⁻³)	T_{dec} (K)	Reference
1. [(CH ₃) ₃ S][FeCl ₄]	315	13	39.7	61.9	1.56	550	This work
2. [(CH ₃) ₄ N][FeCl ₄]	385	5	21.9	32.4	1.48	-	35
3. [(CH ₃) ₃ (CH ₂ Cl)N][FeCl ₄]	329	5	44.0	80.2	1.62	530	5
4. [(CH ₃) ₃ S] ₂ [MnBr ₄]	312	32	23.6	48.8	2.07	519	36
5. [(CH ₃) ₃ S] ₂ [CdBr ₄]	304	32	20.0	45.0	2.25	506	36
6. [(CH ₃) ₃ S] ₂ [ZnBr ₄]	310	37	20.1	42.8	2.13	500	36
7. [Fe(C ₅ (CH ₃) ₄ H) ₂][FeCl ₄]	298	8	16.1	24.0	1.49	-	2
8. [Fe(C ₅ (CH ₃) ₄ H) ₂][GaCl ₄]	301	43	24.4	37.3	1.53	-	2
9. [Fe(C ₅ (CH ₃) ₄ H) ₂][B(CN) ₄]	312	10	34.1	42.3	1.24	-	2
10. [Fe(C ₅ (CH ₃) ₄ H) ₂][C(CN) ₃]	343	18	68	87.7	1.29	525	2
11. [Fe(C ₅ (CH ₃) ₄ H) ₂][(SO ₂ F) ₂ N]	355	21	25.5	41.8	1.64	523	2
12. [C ₅ H ₉ N ₂][FeCl ₄]	357	22	97.7	159.2	1.63	624	37
13. [C ₅ H ₁₄ NO][FeCl ₄]	282	26	38.8	38.4	0.99	520	38

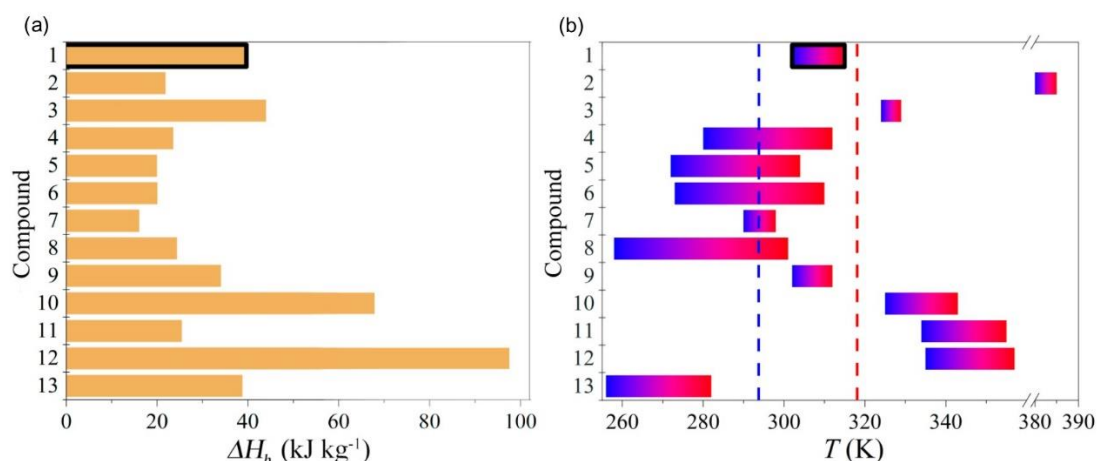


Figure 2. (a) Comparison of latent heat (ΔH) measured on heating for hybrid halometallate compounds. Note: numbers indicate the corresponding hybrid halometallate compounds from Table 1. (b) Comparison of operational temperature for the same compounds. Note: the blue end of the bars indicates the discharging temperature and the red end of the bars indicate the charging temperature. The compound $[(\text{CH}_3)_3\text{S}][\text{FeCl}_4]$ reported in this work is #1 and it is enclosed within a black frame. Dashed lines are guidelines indicating the average discharging (blue) and charging (red) temperatures for solar TES domestic applications.³⁰

3.2. Crystal structures by single-crystal X-ray diffraction

In order to understand the origin of the observed phase transition, single-crystal X-ray diffraction experiments were performed at different temperatures well below and above the transition temperature T_t . The SCXRD results reveal a structural phase transition at T_t from a rather ordered low temperature LT-polymorph present at $T < T_t$ into a highly disordered high temperature HT-polymorph present at $T > T_t$. Even more, this solid-to-solid phase transition is completely reversible, even if the crystals get twinned on phase transition.

The LT-polymorph is orthorhombic, space group $Pnma$ (see more details at Table S1 of SI and Figure 3).

Concerning the molecular arrangement within the crystal structure, the compound displays a NiAs-type structure where the $[\text{FeCl}_4]^-$ anions are surrounded by six $[(\text{CH}_3)_3\text{S}]^+$ cations, forming an octahedral environment, while the $[(\text{CH}_3)_3\text{S}]^+$ cations themselves are surrounded by six $[\text{FeCl}_4]^-$ in a trigonal prismatic environment.

The asymmetric unit of the LT-polymorph consists of one half of $[(\text{CH}_3)_3\text{S}]^+$ and one half of $[\text{FeCl}_4]^-$, as both moieties are placed over a mirror symmetry plane. In the case of this anion, the Fe^{3+} are in a slightly distorted tetrahedral environment as three different Fe-Cl distances are observed (see Figure S4 of SI). It is also worth highlighting that at 100 K both the cationic and anionic species are ordered. On the other hand, the interactions between the anionic-cationic components are electrostatic and weak (see Figure 3). In addition, there are interactions between Cl-atoms of $[\text{FeCl}_4]^-$ entities and H-atoms of methyl groups of $[(\text{CH}_3)_3\text{S}]^+$ (see Figure S4 and Table S2 of SI). At 100K these interactions occur in the bc-plane and involve in particular one of the Cl-atoms (the one with largest Fe-Cl distance) and four methyl groups of three $(\text{CH}_3)_3\text{S}^+$; see Figure S5 of SI.

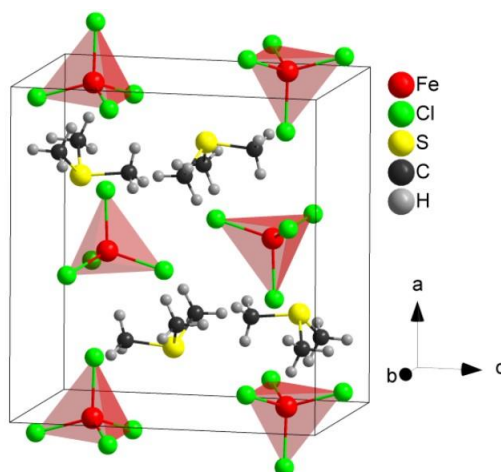


Figure 3. Crystal structure of the LT-polymorph of $[(\text{CH}_3)_3\text{S}][\text{FeCl}_4]$ at 100K.

As for the thermal evolution of the crystal structure of the LT-polymorph from $T = 100 \text{ K}$ to 310 K , our studies confirm that the compound preserves the $Pnma$ symmetry up to T_t .

The unit cell shows some anisotropy in the expansion: the b axis remains almost constant while the a and c axes elongate with temperature, even if the unit cell volume exhibits the expected thermal expansion upon heating (see Figure S6 of SI).

Another interesting feature is that the $[(\text{CH}_3)_3\text{S}]^+$ cations start exhibiting some rotational disorder as soon as temperature increases above 100 K , so that their coordinates can be modelled and refined in 2, or even 4 disordered orientations at 310 K (see Figure S7 and S8 and table S3 of SI).

The increasing number of $[(\text{CH}_3)_3\text{S}]^+$ orientations extends and complicates the hydrogen bonding interaction between the cationic and anion species (table S2 of SI) making them more spherically (isotropically) distributed in space, instead of only restricted to the bc plane.

Above T_t the X-ray diffraction data show a twinning, exhibit strong diffuse scattering (see Figure S9 of SI) and a drastic reduction in Bragg reflection intensity ($\sim 1.35 \text{ \AA}$ maximum resolution observed), as it is characteristic for plastic crystals composed of severely disorder molecular entities.⁴¹ This precluded the refinement of the HT-structure, although the data could be indexed to a cubic symmetry with a primitive cell, with cell parameter $a = 6.662(1) \text{ \AA}$ (Table S1 in SI). The formation of a high-temperature highly disordered phase of cubic symmetry is also typical for plastic crystals.⁴²

The orientational degree of freedom of the $[(\text{CH}_3)_3\text{S}]^+$ and the $[\text{FeCl}_4]^-$ in the HT-polymorph is also supported by the weakly associated anion–cation components and the high latent heat associated to the phase transition, as discussed before.

3.3. Magnetic properties: magnetization results and ESR

The temperature dependence of the magnetic susceptibility of $[(\text{CH}_3)_3\text{S}][\text{FeCl}_4]$ was measured in a wide temperature range across the structural phase transition (Figure 4a). The inverse susceptibility *versus* temperature fits nicely to a Curie law in the temperature range $4.2 < T(\text{K}) < 300$ (Figure 4b), which discards any type of magnetic ordering. The magnetic moment in the LT-polymorph is $\mu \approx 5.8 \mu_B/\text{Fe}$, in good agreement with a spin-only value expected for Fe^{3+} .

In addition, the magnetic susceptibility shows hysteretic behaviour in the temperature range $300\text{--}320 \text{ K}$, i.e. across the first order structural phase transition (see the inset to Figure 4a). On the other hand, the magnetic susceptibility of the HT-polymorph deviates continuously from the Curie law indicating a continuous decrease of the magnetic moment in the plastic crystal phase. The reversible behaviour of the magnetic susceptibility and the TGA analysis discard the evaporation of any of the components of $[(\text{CH}_3)_3\text{S}][\text{FeCl}_4]$ in this temperature range. Thus, the continuous change in the magnetic moment must reflect a variation in the static Fe–Cl (crystal-field) distances.

To access the dynamic magnetic structure of the system in the LT- and HT-polymorphs, we recorded the Electron Spin Resonance (ESR) spectra from 130 K to 400 K .

The low temperature spectrum consists of a single Lorentzian line coming from the resonance of Fe^{3+} (d^5), centered around $H_r \approx 3280 \text{ G}$ ($g \approx 2.07$), and with a linewidth which decreases continuously, from $\Delta H_{pp} \approx 2100 \text{ G}$ at 150 K , to $\Delta H_{pp} \approx 1550 \text{ G}$ at 300 K , right before T_t , see Figure 5.

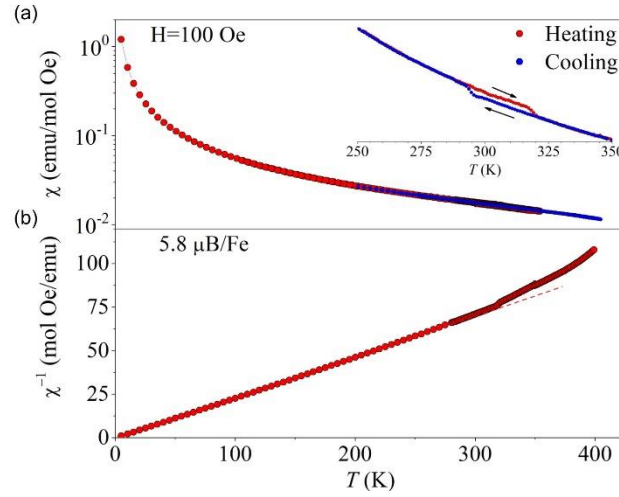


Figure 4. (a) Temperature dependence of the magnetic susceptibility measured at $H = 100$ Oe. The inset shows an enlargement around the structural phase transition. (b) Inverse susceptibility *versus* temperature curve and its fitting to a Curie Law (dash line).

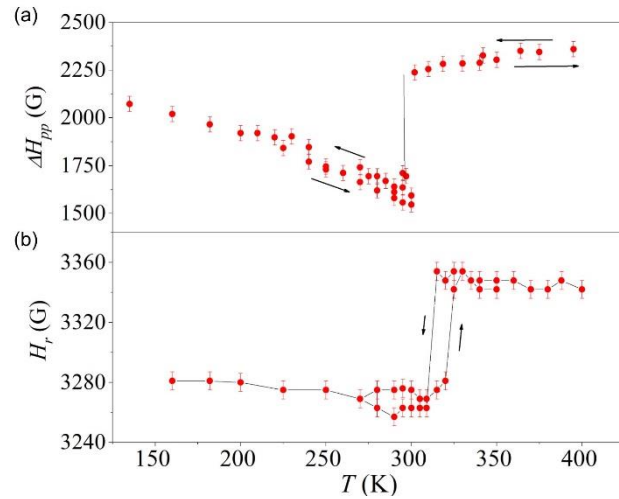


Figure 5. (a) Temperature dependence of the ESR linewidth. (b) Resonance field across the structural phase transition.

Given the large Fe-Fe distances (~ 6.5 - 7.3 Å) in the crystal, dipolar interactions must be the source of line-broadening in this compound with negligible narrowing from direct exchange interaction ($J \approx 0$ from the magnetic susceptibility data).

In this case $\Delta H_{pp} \approx (0.5\pi\mu_{eff}\rho)$, where the effective μ_{eff} is the effective magnetic moment ($5.8 \mu_B$) and ρ is the spin density (3.39×10^{21} Fe/cm³). This calculation predicts a value of $\Delta H_{pp} \approx 2860$ G, about 35% larger than the value of ΔH_{pp} at the lowest temperature measured in this work. Moreover, there is a marked and continuous decrease of ΔH_{pp} with temperature.

There are many intrinsic (dipolar interaction, etc) and extrinsic (vacancies or imperfections, etc) factors which add random perturbations to the local magnetic field sensed by each Fe³⁺ ion, broadening the experimental ESR signal. However, if the resonating spins can move at a faster rate (ω_r) than the amplitude of the perturbations (ω_p), this averages out the effect of the inhomogeneities over the local field, narrowing the ESR absorption line, according to:

$$\Delta\omega = \frac{\omega_{dip}^2}{\omega_r}$$

This is the mechanism responsible for line-narrowing in liquids (due to rapid spin-probe diffusion),⁴³ in doped organic/inorganic semiconductors due to fast polaron diffusion,⁴⁴ and also in plastic crystals, through averaging out of the anisotropic spin environment through fast rotational movement.³⁵

Moreover, fast rotational movement produces a characteristic Lorentzian lineshape, consistent with the experimental observation (pure dipolar interaction between like spins in dense solids results in absorption lines with a characteristic Gaussian shape).⁴⁵

Therefore, the continuously decreasing linewidth observed in the LT-phase is consistent with the motional narrowing from the thermally activated rotation of $[(\text{CH}_3)_3\text{S}]^+$ observed by X-ray diffraction.³⁵

On the other hand, both ΔH_{pp} and H_r show a discontinuous increase at T_t , and remain constant above this temperature in the HT-polymorph, see Figure 5. In this case, the almost constant ΔH_{pp} , $\approx 20\%$ smaller than the calculation, suggests that the mechanism responsible for line-narrowing observed in the LT-polymorph is not operative in the HT-polymorph. Although this result is far from being completely understood, the strong disorder observed in XRD above T_t , as well as the continuous departure observed from the Curie law suggest a diffusive movement of the ionic environment.

3.4. Dielectric properties

To probe the hypothesis of the ionic dynamics, we measured the dielectric properties across the structural transition. Figure 6 shows the temperature dependence of the real part of the complex dielectric permittivity (the so-called dielectric constant or real part of the relative permittivity, ϵ'_r) in the temperature range 300-350 K. As it can be seen, a sharp dielectric transition occurs at $T \sim 318$ K, transforming the ϵ'_r (LT-polymorph) ≈ 10 into ϵ'_r (HT-polymorph) ≈ 45 -50. Therefore, the dielectric constant of the material increases up to 5 times when heating above the phase transition. It should be noted that the relative permittivity is directly related to the capacity of a material to store electrical energy into a parallel plate capacitor. Accordingly, this sharp phase transition involves the increase of up to five times of the amount of electric energy that can be stored into a capacitor built with this material at temperatures above T_t .

On the other hand, and view of the shape of the ϵ'_r versus T curve, which reminds of that shown by antiferroelectric materials, and the crystal structures of both polymorphs, we can rationalize the observed dielectric response as following: it is related to the change from an antiferrodistortive arrangement in the LT-polymorph to a paraelectric state in the HT-polymorph. In this context, a careful inspection of the low temperature crystal structure reveals the existence of two cooperative antiferrodistortive distortions that could be responsible for the subsequent structural and dielectric transition:

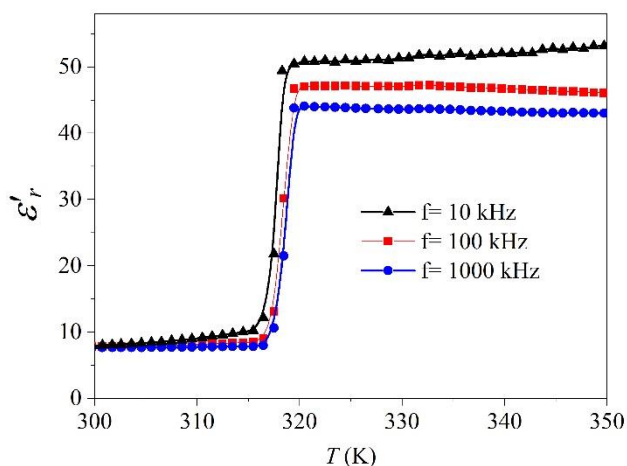


Figure 6. Temperature dependence of the dielectric constant (ϵ'_r), measured at different frequencies (10, 100 and 1000 kHz) for $[(\text{CH}_3)_3\text{S}][\text{FeCl}_4]$.

(i) an off-center shift of the Fe^{3+} cations in the $[\text{FeCl}_4]^-$ anions in the LT-polymorph, which renders these tetrahedral ions polar with an associated electrical dipole of 1.13 D.

Considering that those tetrahedral ions are antiparallely arranged with respect to each other in the crystal, the resulting net polarization nulled, see Figure S10 of SI. (ii) The $[(\text{CH}_3)_3\text{S}]^+$ cations, which are also polar species with an associated dipole moment of 1.21 D, display an antiparallel arrangement in the LT-polymorph, as shown in Figure S10 of SI.

Meanwhile, in the disordered HT polymorph, the moments associated to the moving/rotating ionic species average out, giving rise to a paraelectric state.

Additionally, we have studied the solid-state ionic conductivity, which is closely related to the microscopic rotational and translational motions of the ionic species, see Figure 7. Interestingly, the conductivity of the LT-phase experiences a large variation at T_t , increasing approximately by two orders of magnitude. It is also worth noting that the conductivity of both the LT- and HT-phases

follow an Arrhenius law, see Figure 7. From the linear relationship of $\log \sigma$ versus $1000/T$ data, the activation energies could be calculated as $E_a(\text{LT-polymorph}) = 0.51$ eV and $E_a(\text{HT-polymorph}) = 0.15$ eV.

Within the context discussed before, the lower conductivity of the LT-polymorph is attributed to the restricted ionic movement in an ordered crystalline phase. In contrast, the relatively high conductivity of the HT-polymorph seems to indicate a substantial degree of self-diffusion of the ionic species within this plastic phase, as often observed in ionic plastic crystals.⁴⁶

Given the persistence of (low intensity) X-ray diffraction signal, the HT-phase could be a mesophase with coexistence of crystalline and glassy regions and $[(\text{CH}_3)_3\text{S}]^+$ cations and $[\text{FeCl}_4]^-$ anions could possess an orientational degree of freedom in both of them. In addition, the glassy region seems to show certain translational motions of the ionic species, where the dipolar interaction between the ionic species is temperature independent.

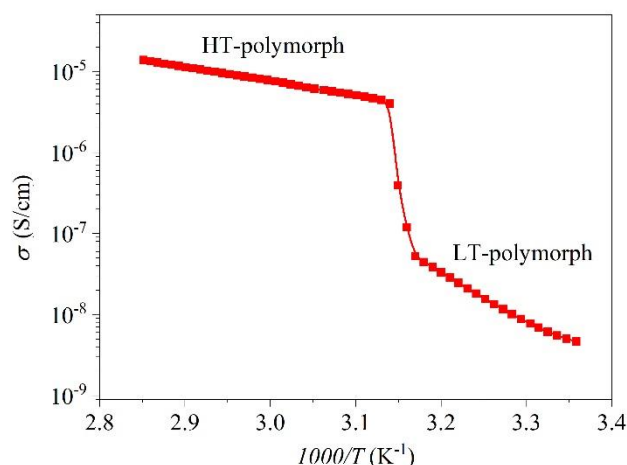


Figure 7. Temperature dependence of conductivity of $[(\text{CH}_3)_3\text{S}][\text{FeCl}_4]$.

Conclusions

In this work we report on a novel plastic crystal $[(\text{CH}_3)_3\text{S}][\text{FeCl}_4]$, which exhibits several interesting functional properties and can also be interesting for multi-energy storage (both thermal energy storage (TES) and electric energy storage). In fact, solar energy cannot only be converted and stored as thermal energy in this material but it also induces a notable increase in the amount of electric energy that can be stored on a capacitor made with this material.

As explained in detail, this compound undergoes a reversible, first-order phase transition near room temperature ($T_t \sim 315$ K), with a rather large thermal hysteresis of 13 K and a notable latent heat ($\Delta H = 39.7$ kJ kg⁻¹) around the phase transition temperature, which render this material very interesting for solar thermal energy storage with an operational temperature for storing and releasing thermal energy between 42 °C (315 K) and 29 °C (302 K), respectively.

The characterization of the solid-solid reversible phase transitions reveals a reversible transformation of a LT-ordered orthorhombic (S.G: *Pnma*) polymorph into a dynamically highly disordered cubic plastic phase, whose detailed characteristics and evolution with temperature we have investigated by SCXRD, ESR, magnetic and dielectric measurements.

Very remarkably this PCM compound exhibits temperature-induced reversible changes in its magnetic, dielectric, and conducting behaviour associated to such phase transition, namely: (i) a hysteretic magnetic behaviour across the transition with decrease of the magnetic moment in the dynamically disordered plastic phase; (ii) a sharp dielectric transition from an antiferrodistortive arrangement in the LT-polymorph to a paraelectric state at the HT-polymorph, and (iii) a sharp increase of the ionic conductivity in the plastic phase probably related to a substantial degree of self-diffusion of the ionic species within that phase.

In the specific case of its dielectric constant, we find that it increases up to five times when heating the material above the phase transition, giving rise to a fivefold increase in the capacity of the material to store electric energy when in the form of a capacitor. Therefore, the provided solar energy can not only be stored as latent heat, but can also induce a fivefold increase in electrical energy that can be stored in a capacitor device made with this material. Therefore we propose $[(\text{CH}_3)_3\text{S}][\text{FeCl}_4]$ as a new material with solar TES and with multiple energy storage capabilities.

Conflicts of interest

There are no conflicts to declare.

Acknowledgements

This work was financially supported by the Ministerio de Economía y Competitividad (MINECO) and EU-FEDER under the project MAT2017-86453-R and Xunta de Galicia under the project ED431G/09. F. R. acknowledges support from the Ministry of Science of Spain (Project No. MAT2016-80762-R), the Consellería de Cultura, Educación e Ordenación Universitaria (ED431F 2016/008, and Centro singular de investigación de Galicia accreditation 2016-2019, ED431G/09), the Xunta de Galicia (ED431B 2018/16) and the European Regional Development Fund (ERDF). J. M. B.-G. acknowledges Xunta de Galicia for a Postdoctoral Fellowship.

References

- 1 J. Estager, J. D. Holbrey and M. Swadźba-Kwaśny, *Chem. Soc. Rev.*, 2014, 43, 847–886.
- 2 T. Mochida, M. Ishida, T. Tominaga, K. Takahashi, T. Sakurai and H. Ohta, *Phys. Chem. Chem. Phys.*, 2018, 20, 3019–3028.
- 3 R. Kore, P. Berton, S. P. Kelley, P. Aduri, S. S. Katti and R. D. Rogers, *ACS Catal.*, 2017, 7, 7014–7028.
- 4 A. W. Taylor, S. Men, C. J. Clarke and P. Licence, *RSC Adv.*, 2013, 3, 9436–9445.
- 5 D. Li, X.-M. Zhao, H.-X. Zhao, L.-S. Long and L.-S. Zheng, *Inorg. Chem.*, 2019, 58, 655–662.
- 6 K. Y. Chan, B. Jia, H. Lin, N. Hameed, J. H. Lee and K. T. Lau, *Compos. Struct.*, 2018, 188, 126–142.
- 7 X. Zhang, X. Wang and D. Wu, *Energy*, 2016, 111, 498–512.
- 8 S. Jang, E. Hwang, Y. Lee, S. Lee and J. H. Cho, *Nano Lett.*, 2015, 15, 2542–2547.
- 9 X. Huang, G. Alva, Y. Jia and G. Fang, *Renew. Sustain. Energy Rev.*, 2017, 72, 128–145.
- 10 X. Geng, W. Li, Y. Wang, J. Lu, J. Wang, N. Wang, J. Li and X. Zhang, *Appl. Energy*, 2018, 217, 281–294.
- 11 K. T. Butler, A. Walsh, A. K. Cheetham and G. Kieslich, *Chem. Sci.*, 2016, 7, 6316–6324.
- 12 H. Y. Ye, J. Z. Ge, Y. Y. Tang, P. F. Li, Y. Zhang, Y. M. You and R. G. Xiong, *J. Am. Chem. Soc.*, 2016, 138, 13175–13178.
- 13 J. Even, M. Carignano and C. Katan, *Nanoscale*, 2016, 8, 6222–6236.
- 14 J. Timmermans, *J. Phys. Chem. Solids*, 1961, 18, 1–8.
- 15 L. A. K. Staveley, *Annu. Rev. Phys. Chem.*, 1962, 13, 351–368.
- 16 M. Ben Bechir, K. Karoui, M. Tabellout, K. Guidara and A. Ben Rhaïem, *J. Alloys Compd.*, 2014, 588, 551–557.
- 17 J. Harada, T. Shimojo, H. Oyamaguchi, H. Hasegawa, Y. Takahashi, K. Satomi, Y. Suzuki, J. Kawamata, and T. Inabe, *Nat. Chem.*, 2016, 8, 946–952.
- 18 J. Harada, N. Yoneyama, S. Yokokura, Y. Takahashi, A. Miura, N. Kitamura, and T. Inabe, *J. Am. Chem. Soc.*, 2018, 140, 1, 346–354.
- 19 J. Harada, Y. Kawamura, Y. Takahashi, Y. Uemura, T. Hasegawa, H. Taniguchi, and K. Maruyama, *J. Am. Chem. Soc.*, 2019, 141, 23, 9349–9357.
- 20 Z. X. Zhang, T. Zhang, P. P. Shi, W. Y. Zhang, Q. Ye and D. W. Fu, *Inorg. Chem. Front.*, 2020, 7, 1239–1249.
- 21 A. Sharma, V. V. Tyagi, C. R. Chen and D. Buddhi, *Renew. Sustain. Energy Rev.*, 2009, 13, 318–345.
- 22 K. Pielichowska and K. Pielichowski, *Prog. Mater. Sci.*, 2014, 65, 67–123.
- 23 A. Fallahi, G. Guldentops, M. Tao, S. Granados-Focil and S. Van Dessel, *Appl. Therm. Eng.*, 2017, 127, 1427–1441.
- 24 S. Sundararajan, A. B. Samui and P. S. Kulkarni, *J. Mater. Chem. A*, 2017, 5, 18379–18396.
- 25 G. Alva, L. Liu, X. Huang and G. Fang, *Renew. Sustain. Energy Rev.*, 2017, 68, 693–706.
- 26 C. Alkan, E. Günther, S. Hiebeler, Ö. F. Ensari and D. Kahraman, *Sol. Energy*, 2012, 86, 1761–1769.
- 27 Y. Zhang, L. Wang, B. Tang, R. Lu and S. Zhang, *Appl. Energy*, 2016, 184, 241–246.
- 28 X. Du, H. Wang, Y. Wu, Z. Du and X. Cheng, *J. Appl. Polym. Sci.*, 2017, 134, 1–8.
- 29 L. Navarro, A. de Gracia, S. Colclough, M. Browne, S. J. McCormack, P. Griffiths and L. F. Cabeza, *Renew. Energy*, 2016, 88, 526–547.
- 30 F. Souayfane, F. Fardoun and P.-H. Biwole, *Energy Build.*, 2016, 129, 396–431.
- 31 Y. Huang, M. Zhu, Y. Huang, Z. Pei, H. Li, Z. Wang, Q. Xue and C. Zhi, *Adv. Mater.*, 2016, 28, 8344–8364.
- 32 C. F. Macrae, I. Sovago, S. J. Cottrell, P. T. A. Galek, P. McCabe, E. Pidcock, M. Platings, G. P. Shields, J. S. Stevens, M. Towler and P. A. Wood, *J. Appl. Crystallogr.*, 2020, 53, 226–235.
- 33 G. M. Sheldrick and IUCr, *Acta Crystallogr. Sect. A Found. Adv.*, 2015, 71, 3–8.
- 34 G. M. Sheldrick, *Acta Crystallogr. Sect. C Struct. Chem.*, 2015, 71, 3–8.
- 35 J. Salgado-Beceiro, S. Castro-García, M. Sánchez-Andújar and F. Rivadulla, *J. Phys. Chem. C*, 2018, 122, 27769–27774.
- 36 X. G. Chen, Y. Z. Zhang, D. S. Sun, J. X. Gao, X. N. Hua and W. Q. Liao, *Dalt. Trans.*, 2019, 48, 11292–11297.
- 37 A. García-Saiz, P. Migowski, O. Vallcorba, J. Junquera, J. A. Blanco, J. A. González, M. T. Fernández-Díaz, J. Rius, J. Dupont, J. Rodríguez Fernández and I. De Pedro, *Chem. - A Eur. J.*, 2014, 20, 72–76.
- 38 I. De Pedro, A. García-Saiz, J. González, I. Ruiz De Larramendi, T. Rojo, C. A. M. Afonso, S. P. Simeonov, J. C. Waerenborgh, J. A. Blanco, B. Ramajo and J. R. Fernández, *Phys. Chem. Chem. Phys.*, 2013, 15, 12724–12733.

- 39 L. Klimeš, P. Charvát, M. Mastani Joybari, M. Zálešák, F. Haghighat, K. Panchabikesan, M. El Mankibi and Y. Yuan, *Appl. Energy*, 2020, 263, 114572.
- 40 E. Moreles, G. Huelsz and G. Barrios, *Build. Simul.*, 2018, 11, 519–531.
- 41 P. Gerlach and W. Prandl, *Acta Crystallogr. Sect. A Found. Crystallogr.*, 1988, 44, 128–136.
- 42 R. M. Lynden-Bell and K. H. Michel, *Rev. Mod. Phys.*, 1994, 66, 721–762.
- 43 John E. Wertz and J. R. Bolton, *Electron spin resonance : elementary theory and practical applications*, McGraw-Hill, New York, 1972.
- 44 H. Matsui, T. Hasegawa, Y. Tokura, M. Hiraoka and T. Yamada, *Phys. Rev. Lett.*, 2008, 100, 126601.
- 45 C. P. Poole, *Electron spin resonance : a comprehensive treatise on experimental techniques*, Dover Publications, New York, 1983.
- 46 J. M. Pringle, P. C. Howlett, D. R. MacFarlane and M. Forsyth, *J. Mater. Chem.*, 2010, 20, 2056.

Supplementary Information

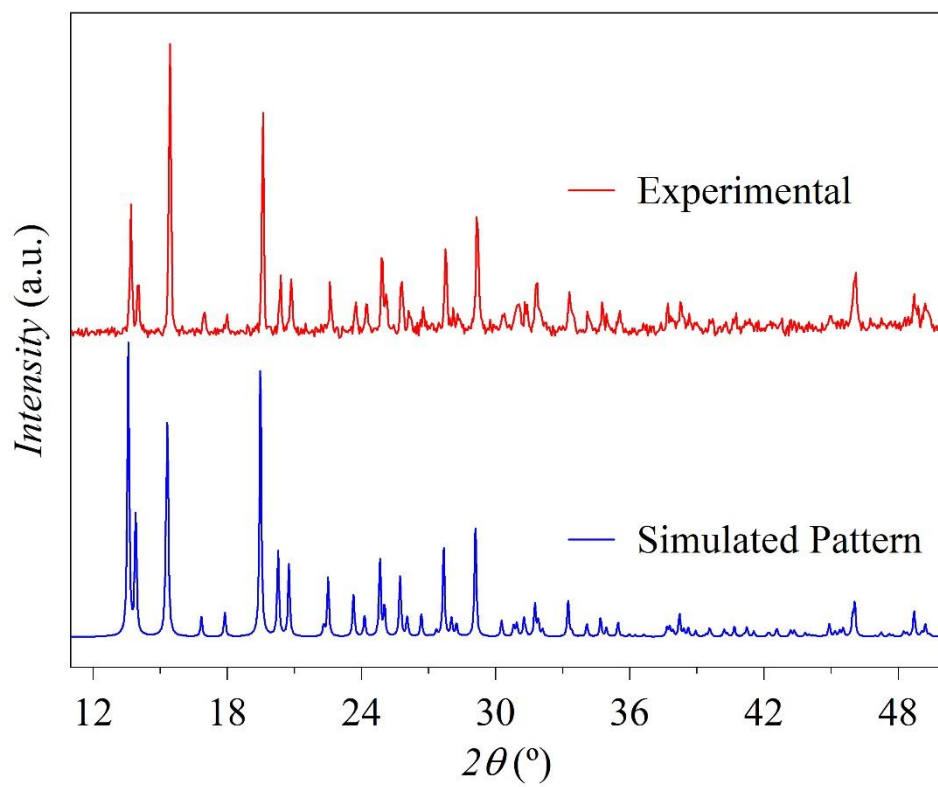


Figure S1. Room temperature experimental PXRd patterns for the obtained $[(CH_3)_3S][FeCl_4]$ compound together with the simulated patterns based on its single crystal structure at room temperature.

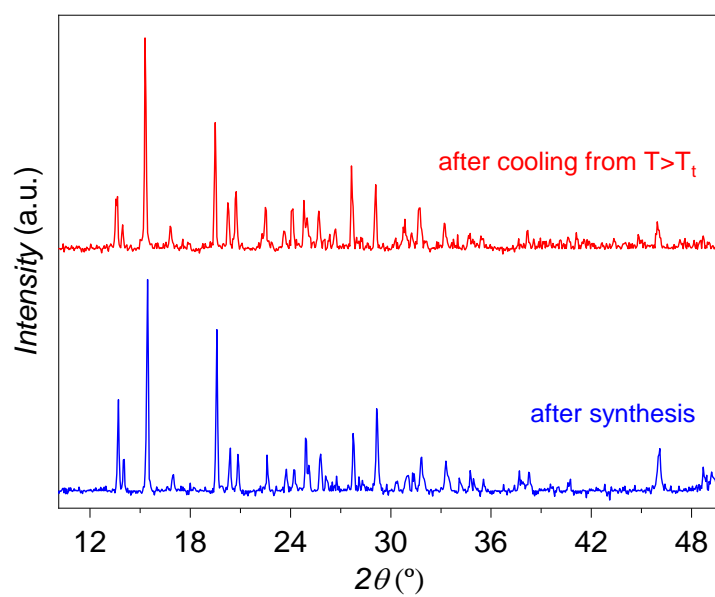
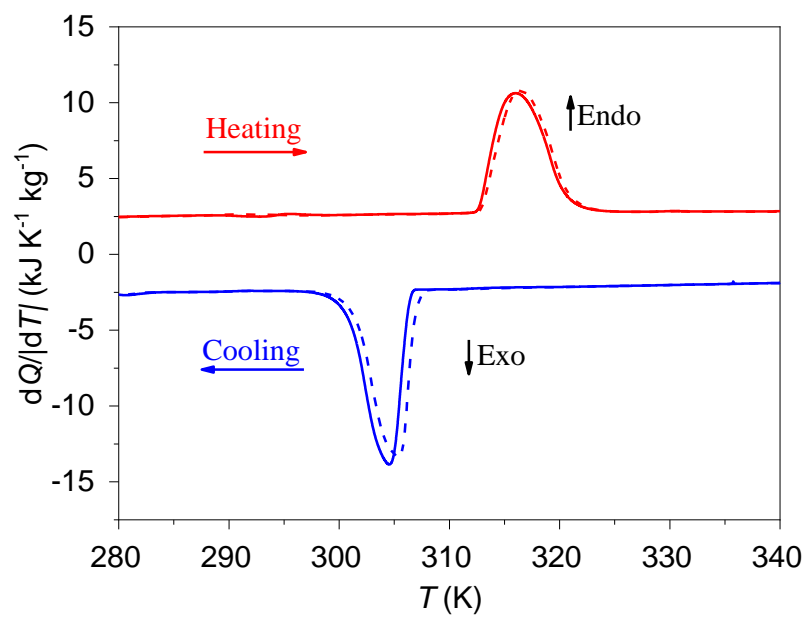


Figure S2. Top) Several DSC curves (solid line first cycle and dash line second cycle) for $[(\text{CH}_3)_3\text{S}][\text{FeCl}_4]$ compound. b) Room temperature PXRD patterns for the obtained $[(\text{CH}_3)_3\text{S}][\text{FeCl}_4]$ compound after synthesis (blue line) and after cooling from $T > T_t$ (red line).

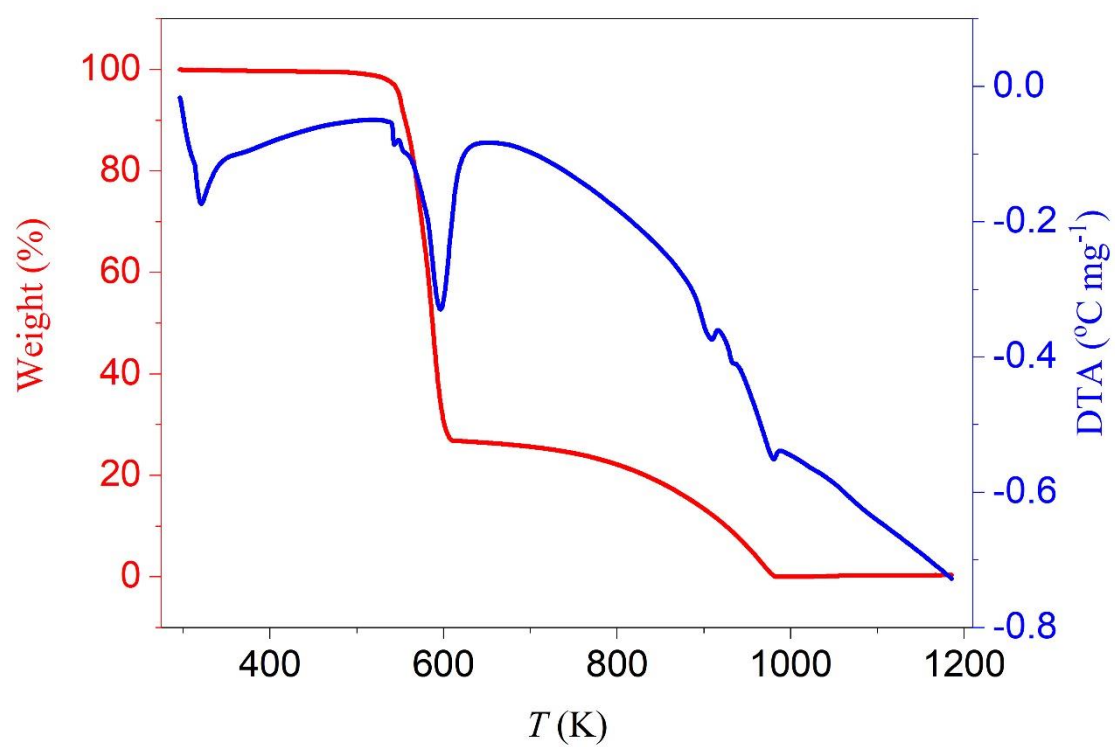


Figure S3. TGA and DTA decomposition curves for the $[(\text{CH}_3)_3\text{S}][\text{FeCl}_4]$ compound.

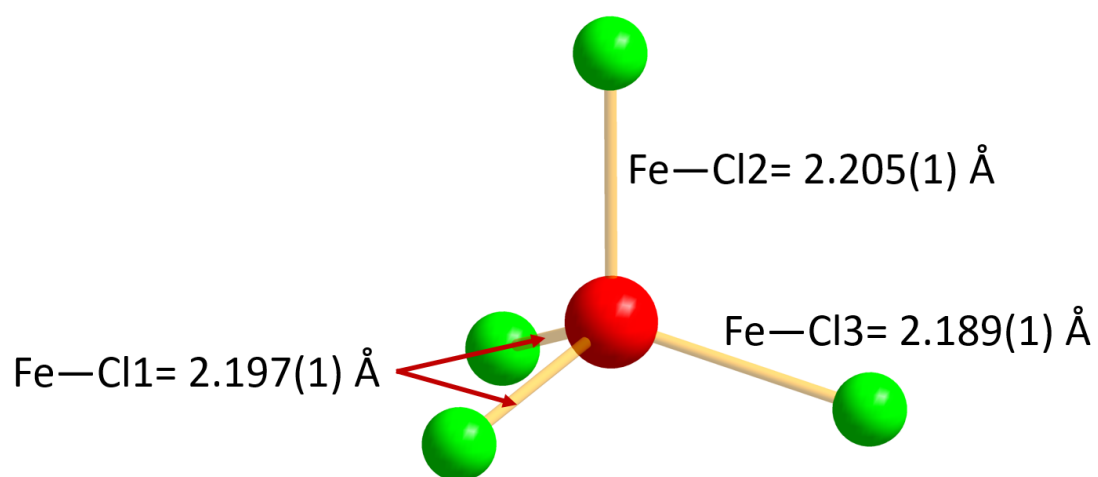


Figure S4. Detail of the crystal structure of the $[(\text{CH}_3)_3\text{S}][\text{FeCl}_4]$ compound showing the three different Fe-Cl distances present in the $[\text{FeCl}_4]^-$ anions at 100K.

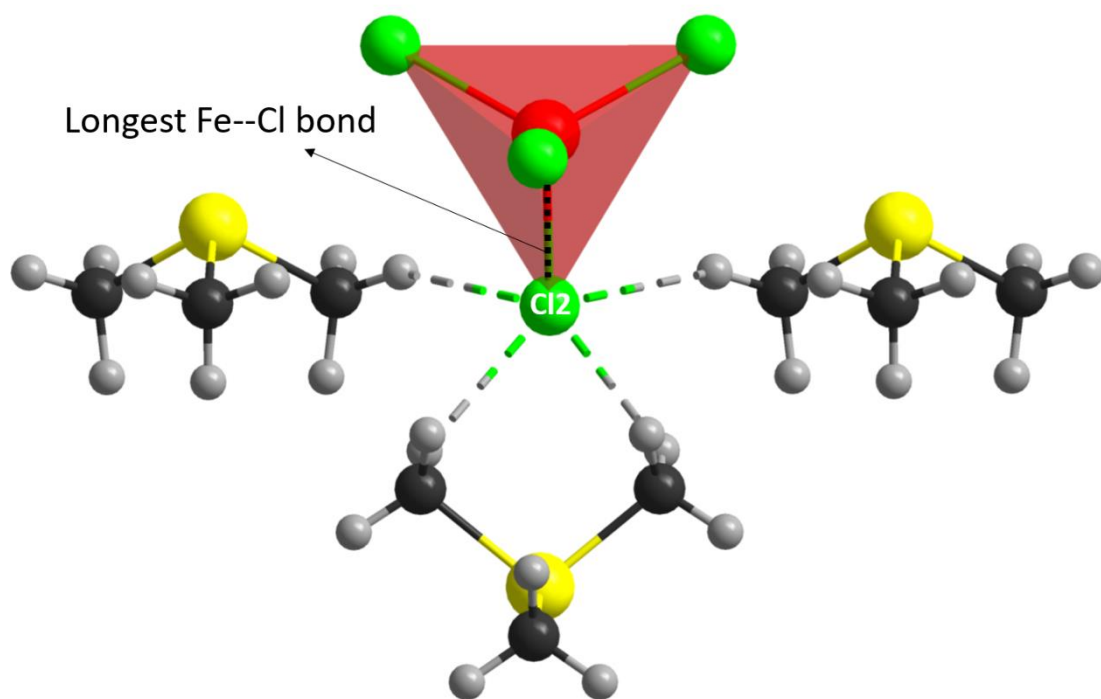


Figure S5. Detail of the crystal structure of the $[(\text{CH}_3)_3\text{S}][\text{FeCl}_4]$ compound at 100K showing the interactions between one Cl-atom of $[\text{FeCl}_4]^-$ with four H-atoms of methyl groups of three $[(\text{CH}_3)_3\text{S}]^+$ cations.

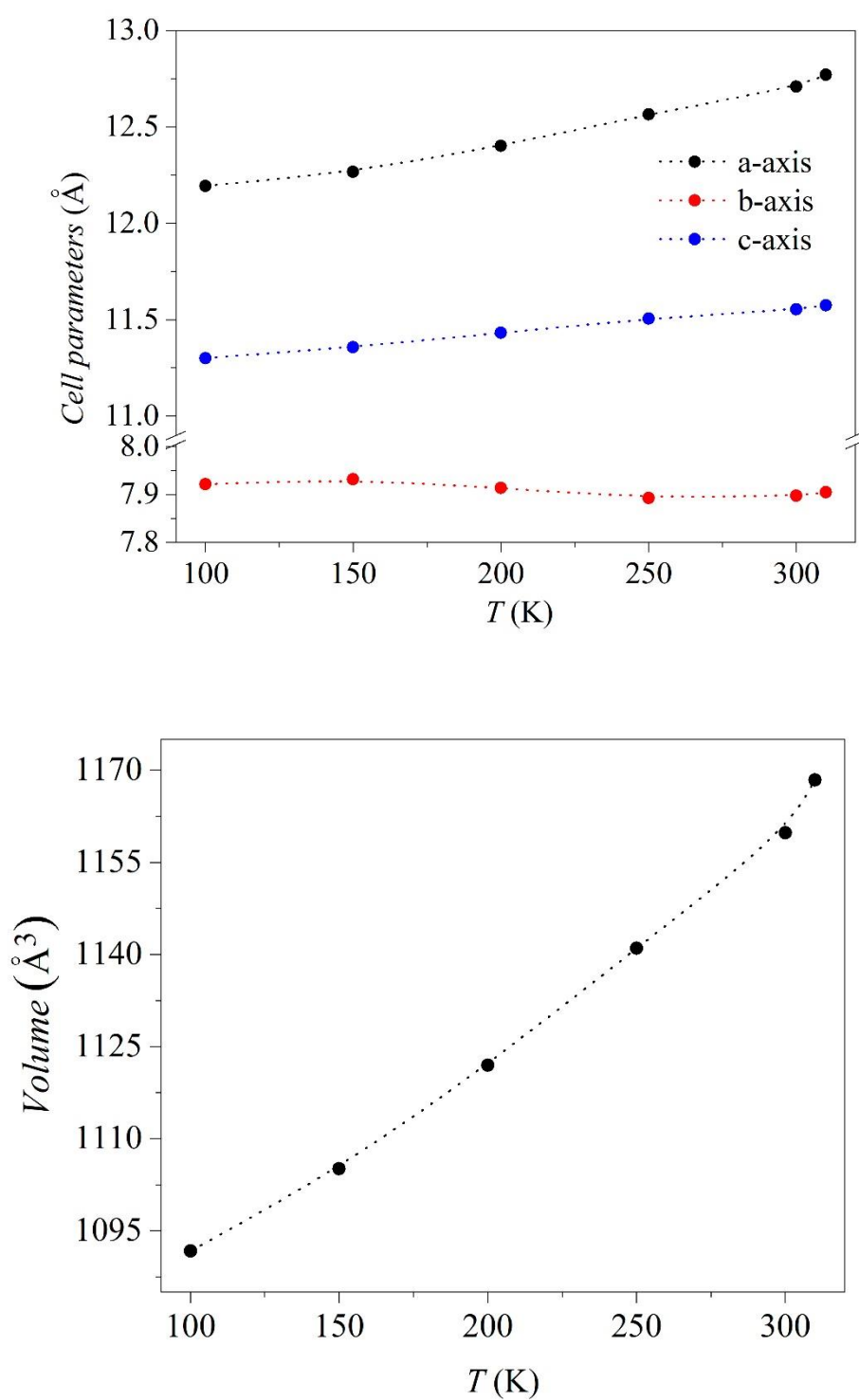


Figure S6. Top: Thermal evolution of the cell parameters of the LT-polymorph of $[(CH_3)_3S][FeCl_4]$. **Bottom:** Thermal evolution of the volume of the LT-polymorph of $[(CH_3)_3S][FeCl_4]$.

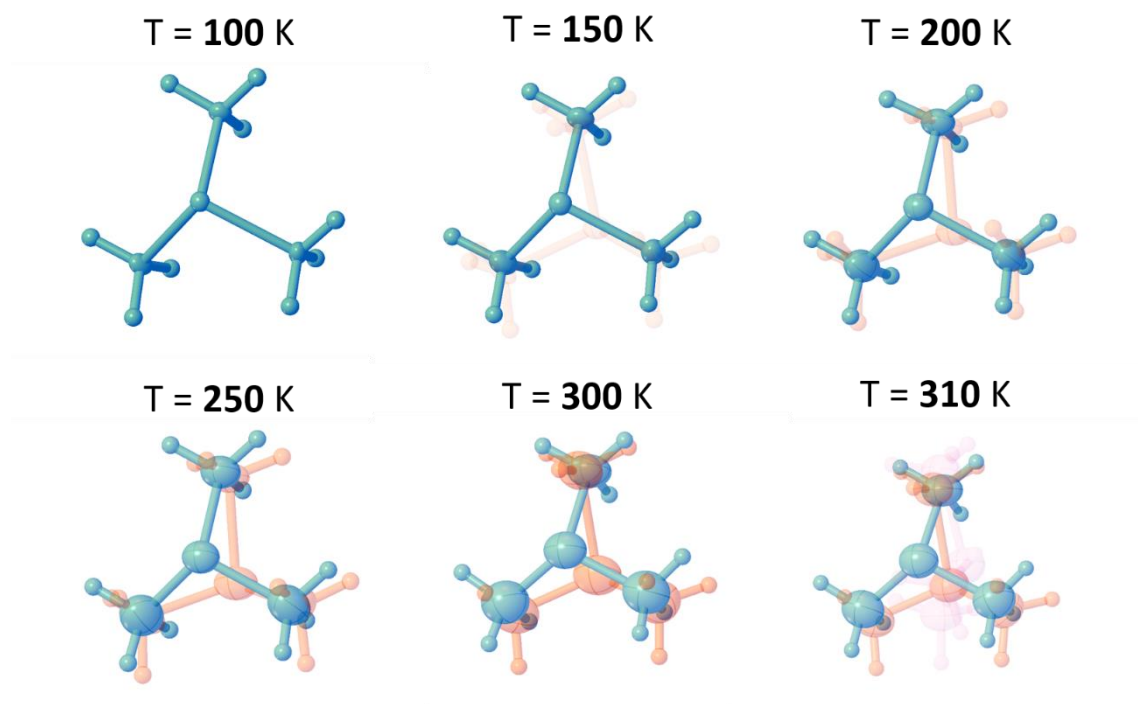


Figure S7. Detail of the crystal structure of $[(\text{CH}_3)_3\text{S}][\text{FeCl}_4]$ showing the disorder of the $[(\text{CH}_3)_3\text{S}]^+$ cations at different temperatures between 100, 150, 200, 250, 300 and 310K (from left top to right bottom). The ellipsoid shows a probability of 30%. Hydrogen atoms shown as spheres of fixed radius. Refined atomic population parameters are used for transparency level (%), see Table S3 for numerical values.

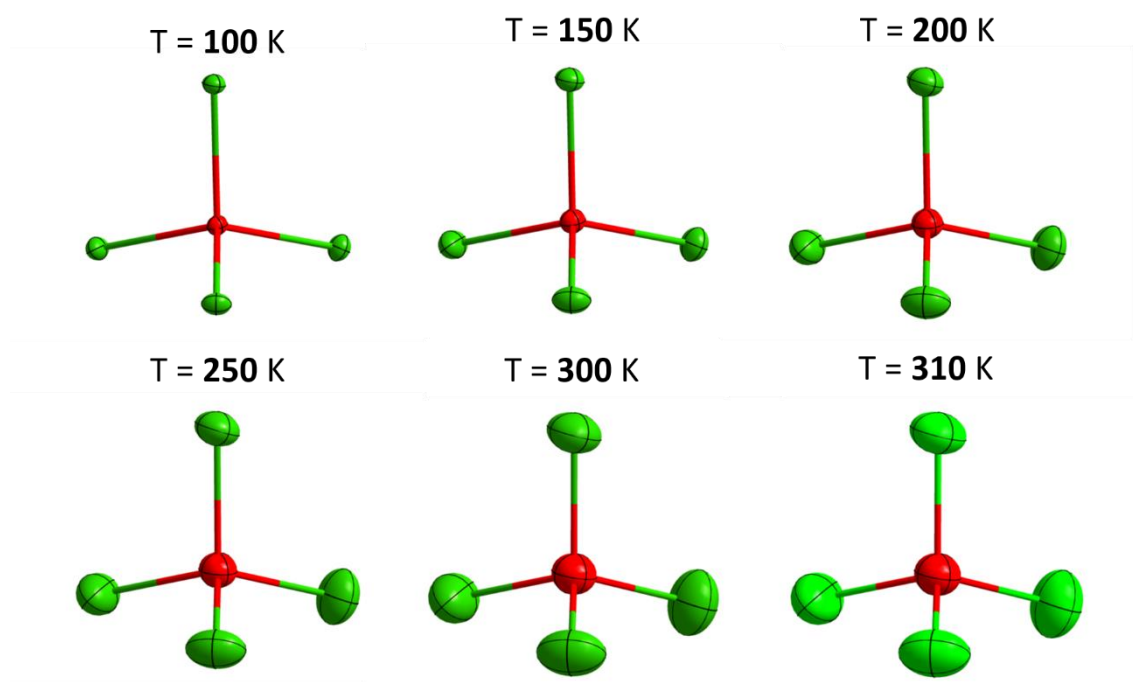


Figure S8. Detail of the crystal structure of $[\text{FeCl}_4]^-$ tetrahedral at different temperatures between 100, 150, 200, 250, 300 and 310 K (from left top to right bottom). The ellipsoid shows a probability of 30%.

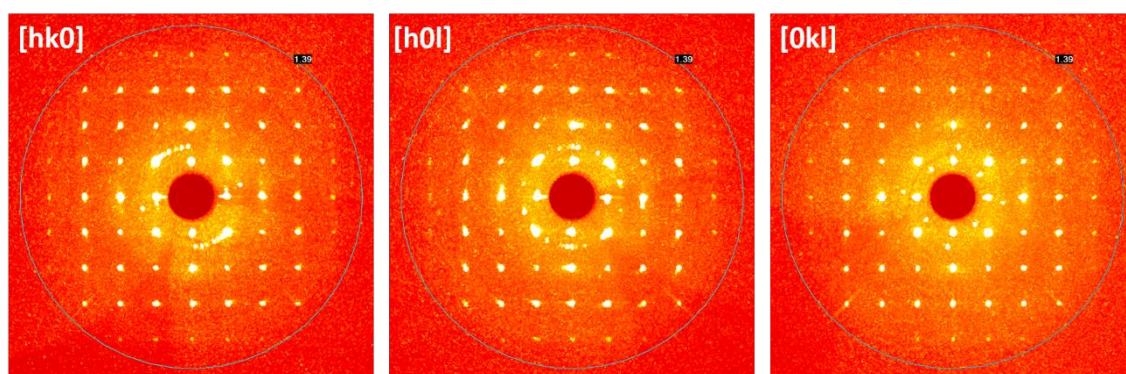


Figure S9. Precession images generated from single-crystal X-ray diffraction data of the HT-polymorph obtained along the main axis.

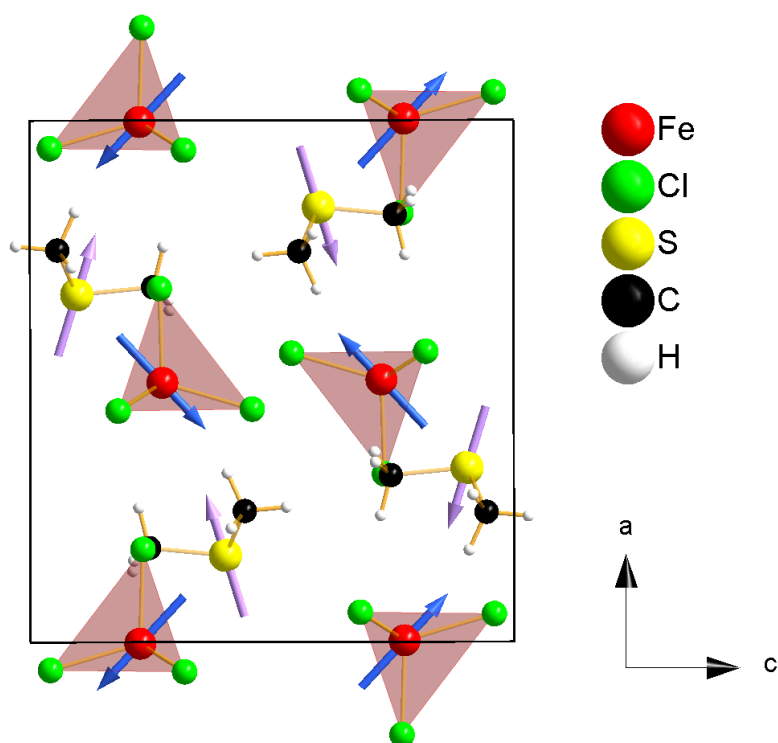


Figure S10. Crystal structure of the LT-polymorph of $[(\text{CH}_3)_3\text{S}][\text{FeCl}_4]$ along the b-axis. The arrows depict the electric dipole of $[(\text{CH}_3)_3\text{S}]^+$ cations (1.21 D) and $[\text{FeCl}_4]^-$ anions (1.13 D). The magnitude and orientation of electric dipole was estimated using the GUASSIAN 09 software.¹ The size of the arrows is unscaled.

¹ Frisch, M. J.; Trucks, G. W.; Schlegel, H. B.; Scuseria, G. E.; Robb, M. A.; Cheeseman, J. R.; Scalmani, G.; Barone, V.; Mennucci, B.; Petersson, G. A. et al. Gaussian 09, Revision E.01, Gaussian, Inc.: Wallingford CT. 2009.

Table S1. Crystal data and structure refinement for [(CH₃)₃S]][FeCl₄].

Empirical formula	C ₃ H ₉ S FeCl ₄						
Wavelength (Å)	0.71073						
Crystal size (mm ³)	0.170 x 0.100 x 0.056						
Formula weight	274.81						
F(000)	548						
							Proposed SG
Temperature (K)	100	150	200	250	300	310	320
Crystal system	Orthorhombic	Orthorhombic	Orthorhombic	Orthorhombic	Orthorhombic	Orthorhombic	Cubic?
Space group	<i>Pnma</i>	<i>Pnma</i>	<i>Pnma</i>	<i>Pnma</i>	<i>Pnma</i>	<i>Pnma</i>	<i>Pm-3m</i> ?
Unit cell dimensions (Å)	a = 12.1950(7)	a = 12.2667(8)	a = 12.4012(4)	a = 12.5644(5)	a = 12.707(4)	a = 12.7698(9)	a = 6.6626(13)
	b = 7.9217(4)	b = 7.9320(5)	b = 7.9136(2)	b = 7.8927(3)	b = 7.900(2)	b = 7.9044(5)	
	c = 11.3013(6)	c = 11.3580(7)	c = 11.4326(4)	c = 11.5059(4)	c = 11.551(4)	c = 11.5756(8)	
Volume (Å ³)	1091.71(10)	1105.13(12)	1121.97(6)	1141.01(7)	1159.6(6)	1168.41(14)	295.75(17)
Z	4	4	4	4	4	4	1
Density calculated (Mg/m ³)	1.672	1.652	1.627	1.600	1.574	1.562	-
Absorption coefficient (mm ⁻¹)	2.482	2.452	2.415	2.375	2.337	2.319	2.290
Tmin, Tmax	0.72, 0.87	0.65, 0.88	0.74, 0.88	0.74, 0.88	0.74, 0.88	0.72, 0.88	0.61, 0.82
Theta range for data collection (°)	2.46 - 36.37	2.44 - 33.16	2.42 - 33.13	2.40 - 29.57	2.38 - 27.13	2.38 - 26.72	3.06 – 15.15

Index ranges	-20<=h<=20 -13<=k<=13 -18<=l<=18	-17<=h<=18 -12<=k<=12 -17<=l<=17	-17<=h<=19 -12<=k<=12 -17<=l<=17	-16<=h<=17 -10<=k<=10 -15<=l<=15	-15<=h<=16 -10<=k<=10 -14<=l<=14	-15<=h<=16 -10<=k<=9 -14<=l<=14	-4<=h<=4 -4<=k<=4 -4<=l<=4
Measured reflections	65618	16182	17487	13914	11340	11256	2763
Independent reflections	2802 [R(int)=0.0488]	2241 [R(int)=0.0417]	2260 [R(int)=0.0369]	1702 [R(int)=0.0390]	1372 [R(int)=0.0365]	1324 [R(int)=0.0332]	24 [R(int)=0.0588]
Indep. Reflections [$I > 2\sigma(I)$]	2420	1726	1715	1194	889	844	24
Completeness (%)	99.8	99.9	99.8	99.8	99.9	99.9	100
Refinement method	Full-matrix least-squares on F ²						-
Data / restraints / parameters	2802 / 0 / 63	2241 / 94 / 83	2260 / 94 / 83	1702 / 94 / 83	1372 / 94 / 83	1324 / 219 / 121	-
Goodness-of-fit on F²	1.102	1.057	1.031	1.022	1.030	1.050	-
Final R indices [$I > 2\sigma(I)$]	R1 = 0.0288 wR2 = 0.0603	R1 = 0.0345 wR2 = 0.0601	R1 = 0.0343 wR2 = 0.0719	R1 = 0.0401 wR2 = 0.0938	R1 = 0.0484 wR2 = 0.1254	R1 = 0.0378 wR2 = 0.0933	-
R indices (all data)	R1 = 0.0377 wR2 = 0.0652	R1 = 0.0542 wR2 = 0.0680	R1 = 0.0514 wR2 = 0.0827	R1 = 0.0602 wR2 = 0.1090	R1 = 0.0764 wR2 = 0.1493	R1 = 0.0621 wR2 = 0.1113	-
Largest diff. peak and hole (e⁻Å⁻³)	0.628 and -0.657	0.652 and -0.469	0.439 and -0.410	0.560 and -0.374	0.522 and -0.262	0.230 and -0.215	-

Table S2. Interactions between Cl-atoms of $[\text{FeCl}_4]^-$ with t H-atoms of methyl group of $[(\text{CH}_3)_3\text{S}]^+$ cations at different temperatures (distances in Å, °). Atoms labelled as ^a, ^b or ^c according to different disordered positions for the cation.

	D-H	H...A	D...A	<(DHA)	
T=100K	0.97(2)	2.79(2)	3.6488(15)	147.0(17)	C1-H1B...Cl2_i
	0.92(2)	2.79(2)	3.6251(15)	150.9(17)	C1-H1C...Cl2_ii
T=150K	0.98	2.84	3.676(6)	144.0	C1^a-H1B^a...Cl2_i
	0.98	2.75	3.632(6)	150.0	C1^a-H1C^a...Cl2_iii
	0.98	3.00	3.73(6)	132.4	C1B^b-H1D^b...Cl2_iii
	0.98	2.72	3.46(5)	132.2	C1B^b-H1D^b...Cl3
	0.98	2.67	3.55(6)	149.1	C1B^b-H1E^b...Cl2_i
	0.98	2.92	3.63(5)	129.5	C1B^b-H1F^b...Cl1_iv
	0.965(19)	2.97(3)	3.64(6)	128(3)	C2B^b-H2E^b...Cl1_iii
T=200K	0.98	2.87	3.675(7)	140.5	C1^a-H1B^a...Cl2_i
	0.98	2.78	3.674(7)	152.5	C1^a-H1C^a...Cl2_iii
	0.98	2.83	3.59(2)	135.0	C1B^b-H1D^b...Cl2_iii
	0.98	2.88	3.547(16)	126.2	C1B^b-H1D^b...Cl3
	0.98	2.87	3.73(2)	147.9	C1B^b-H1E^b...Cl2_i
T=250K	0.97	2.88	3.630(15)	134.4	C1^a-H1B^a...Cl1_iv
	0.97	2.95	3.697(14)	134.8	C1^a-H1B^a...Cl2_i
	0.97	2.81	3.704(14)	154.0	C1^a-H1C^a...Cl2_iii
	0.97	2.84	3.63(3)	139.5	C1B^b-H1D^b...Cl2_iii
	0.97	2.93	3.50(3)	118.3	C1B^b-H1D^b...Cl3
	0.97	2.95	3.75(3)	141.1	C1B^b-H1E^b...Cl2_i
T=300K	0.96	2.75	3.576(15)	144.6	C1^a-H1B^a...Cl1_iv
	0.96	2.80	3.702(18)	157.4	C1^a-H1C^a...Cl2_iii
	0.96	2.77	3.44(2)	127.8	C1B^b-H1D^b...Cl3
	0.96	2.84	3.70(3)	149.5	C1B^b-H1E^b...Cl2_i
	0.94(2)	2.98(3)	3.65(3)	129.6(17)	C2B^b-H2E^b...Cl1_iii
T=310K	0.96	2.81	3.585(11)	138.0	C1^a-H1B^a...Cl1_iv
	0.96	2.84	3.707(14)	150.0	C1^a-H1C^a...Cl2_iii
	0.96	2.69	3.43(2)	134.9	C1B^b-H1D^b...Cl3
	0.96	2.79	3.69(3)	155.7	C1B^b-H1E^b...Cl2_i
	0.96	2.53	3.35(5)	143.4	C1C^c-H1I^c...Cl1_iii
	0.96	2.81	3.72(6)	158.3	C2C^c-H1J^c...Cl1_v
	0.96	2.71	3.48(7)	137.3	C2C^c-H1L^c...Cl1_iii
	0.96	2.92	3.70(6)	138.6	C3C^c-H1M^c...Cl1
	0.96	2.81	3.44(4)	124.6	C3C^c-H1O^c...Cl3_i

Symmetry operations:

- (i) -x+1, -y+1, -z+1
- (ii) x-1/2, -y+3/2, -z+1/2
- (iii) x-1/2, y, -z+1/2
- (iv) -x+1/2, -y+1, z+1/2
- (v) x-1/2, -y+1/2, -z+1/2

Table S3. $[(\text{CH}_3)_3\text{S}]^+$ cation disorder vs temperature.

Temperature (K)	No disordered positions	Refined population parameters (%)
100	1*	100
150	2	92.3(2) / 7.7(2)
200	2	81.1(2) / 18.9(2)
250	2	71.4(3) / 28.6(3)
300	2	65.2(5) / 34.8(5)
310	4	60.0(3) / 25.7(3) / 7.11(14) / 7.11(14)**

(*) There are some low electron density residual peaks in the Fourier difference map that allow to construct and refine (with many constrains) a disordered model for $[(\text{CH}_3)_3\text{S}]^+$ in 2 orientations like that found at higher temperatures. The final refined population parameters are 99.07(13) / 0.93(13) %. It is a much more complicated model with no significant improvement in data fitting, therefore, the no disordered model is considered in the final refinement reported at 100K.

(**) Last two population values are identical because they correspond to disordered positions related by a mirror symmetry plane.

Preprint_Multifunctional TES.pdf (2.00 MiB)

[view on ChemRxiv](#) • [download file](#)
